

# Stellar Wind Accretion in GX301-2: Evidence for a High-density Stream

D.A. Leahy and M.Kostka

*Department of Physics & Astronomy, University of Calgary, Calgary, AB, Canada, T2N 1N4*

## ABSTRACT

The X-ray binary system GX301-2 consists of a neutron star in an eccentric orbit accreting from the massive early-type star WRAY 977. It has previously been shown that the X-ray orbital light curve is consistent with existence of a gas stream flowing out from WRAY 977 in addition to its strong stellar wind. Here, X-ray monitoring observations by the Rossi X-ray Timing Explorer (RXTE)/All-Sky-Monitor (ASM) and pointed observations by the RXTE/Proportional Counter Array (PCA) over the past decade are analyzed. We analyze both the flux and column density dependence on orbital phase. The wind and stream dynamics are calculated for various system inclinations, companion rotation rates and wind velocities, as well as parametrized by the stream width and density. These calculations are used as inputs to determine both the expected accretion luminosity and the column density along the line-of-sight to the neutron star. The model luminosity and column density are compared to observed flux and column density vs. orbital phase, to constrain the properties of the stellar wind and the gas stream. We find that the change between bright and medium intensity levels is primarily due to decreased mass loss in the stellar wind, but the change between medium and dim intensity levels is primarily due to decreased stream density. The mass-loss rate in the stream exceeds that in the stellar wind by a factor of  $\sim 2.5$ . The quality of the model fits is significantly better for lower inclinations, favoring a mass for WRAY 977 of  $\sim 53 - 62M_{\odot}$ .

*Subject headings:* stars: neutron – stars: individual: GX301-2 – stars: emission line, Be – X-rays: stars

## 1. Introduction

GX 301-2 (also known as 4U 1223-62) is a pulsar with a 680 s rotation period, in a 41.5 day eccentric orbit (Sato et al. 1986). The mass function is  $31.8M_{\odot}$ , making the minimum

companion mass  $35M_{\odot}$  for a  $1.4M_{\odot}$  neutron star. The companion Wray 977 has a B1 Ia+ spectral classification (Kaper et al. 1995), determined via comparison with the hypergiant  $\zeta^1$  Sco. This analysis also yielded an upper limit for the radius of Wray 977 of  $75R_{\odot}$  placing it just inside its tidal radius.

The neutron star flares regularly in X-rays approximately 1-2 days before periastron passage, and several stellar wind accretion models have been proposed to explain the magnitude of the flares and their orbital phase dependence (e.g. Koh et al., 1997, Leahy, 1991, Haberl, 1991). The modeling by Leahy (1991) and Haberl (1991) was done using TENMA and EXOSAT observations, respectively, which cover many short data sets spaced irregularly over orbital phase. More recently better orbital phase coverage has been obtained by CGRO/BATSE (Koh et al. 1997), which however has much lower sensitivity than the previous studies.

The broad band X-ray spectrum of GX301-2 has been studied by TENMA (Leahy & Matsuoka, 1990, Leahy & Matsuoka, 1989a and Leahy & Matsuoka, 1989b) and ASCA measurements (Saraswat et al. 1996). The latter study illustrates the complexity of the GX301-2 spectrum. Four components are necessary: i) an absorbed power law with high column density; ii) a scattered power law with much lower column density; iii) a thermal component with temperature of 0.8 keV; iv) a set of six emission lines (including the iron line at 6.4 keV). Of the above, components ii) and iv) are due to reprocessing in the gas in stellar wind from Wray 977 which surrounds the x-ray source. Reprocessed spectra were calculated for a centrally illuminated cloud by (Leahy and Creighton 1993) and for an externally illuminated cloud by (Leahy 1999), including the Comptonized iron line shapes. Later, the Comptonized iron line was detected in GX301-2 using the Chandra High Energy Transmission Grating (Watanabe et al. 2003), confirming the high column density (on the order of  $10^{24}$  cm $^{-2}$ ) and yielding an upper limit on electron temperature of  $\sim 3$  eV. The orbital phase dependence of the X-ray spectrum of GX301-2 was observed by the PCA on board RXTE (Mukherjee and Paul 2004). It was concluded that clumpiness in the matter surrounding the neutron star caused large variability in column density measurements.

Long-term monitoring of GX301-2 has been carried out by the ASM on board RXTE. Analysis of these observations for the 5 year time period MJD 50087.2 to MJD 52284.5 was done by (Leahy 2002) (henceforth referred to as L02). In this paper the light curve based on the significantly longer 10 year RXTE/ASM database is analyzed. In addition we study the flux and column density measurements made by the RXTE/PCA, as well as column densities derived from the RXTE/ASM softness ratios. Improved modeling methods are introduced: accurate analytic description of the stream and inclusion of simultaneous flux and column density calculations. The inclusion of this much more extensive data and

the more realistic modeling results in significant improvement on constraints on the system properties of GX301-2 and allows new conclusions to be drawn.

## 2. RXTE/ ASM and RXTE/ PCA Observations

The ASM on RXTE (Levine et al. 1996) consists of three scanning shadow cameras (SSC's), each with a field of view of  $6^\circ$  by  $90^\circ$  FWHM. The SSC's are rotated in a sequence of “dwells” with an exposure typically of 90 seconds, so that the most of the sky can be covered in one day. The dwell data are also averaged for each day to yield a daily-average. The RXTE/ ASM dwell data and daily-average data were obtained from the ASM web site. The data reduction to obtain the count rates and errors from the satellite observations was carried out by ASM/RXTE team, and the procedures are described at the web site. The ASM count rates used here include the full energy range band as well as the three sub-bands 1.3-3.0 keV, 3.0-5.0 keV and 5.0-12.1 keV. The data covered the time period MJD 50172.6 to MJD 53978.6. The regular outbursts every 41.5 day orbital cycle are seen in the 5-12 keV count rates, as well as the variability from cycle to cycle.

The orbital parameters of GX301-2, updated with the BATSE observations (Koh et al. 1997) and used for the current study are as follows.  $P_{\text{orb}} = 41.498\text{days}$ ,  $a_x \sin(i) = 368.3\text{lt-s}$ , eccentricity  $e = 0.462$ , longitude of periastron  $\omega = 310^\circ$ , time of periastron passage  $T_0 = \text{MJD } 48802.79$ .

The dwell data is used in the analysis that follows. The three RXTE/ ASM sub-bands and full energy range band were epoch folded. The orbital light curves for these bands and the full energy range band are shown in Fig. 1 with orbital phase zero defined by the time of periastron passage,  $T_0$ .

GX301-2 shows a significant variability above statistical uncertainties in intensity from orbit to orbit. This is illustrated in Fig. 2 which shows the RXTE/ ASM data over the entire observation period with timebins equal to one orbital period. The r.m.s. variability is 0.33 ASM c/s compared to a mean error of 0.044 ASM c/s: the variability is real at greater than 7 sigma significance. There is a secular decrease in the mean flux in the amount of -0.07 ASM c/s/year. However the length of the data set is not long enough to establish a long term trend, and the flux is also consistent with no secular decrease after  $\sim \text{MJD } 51200$ . The high time-resolution data were tested for long term periodicities by examining  $\chi^2$  vs. period for epoch folding over periods up to 500 days. This showed peaks at N times the orbital period (with N=1, 2, 3, 4 ...): this is due to aliasing of the orbital light curve. To negate the effect of aliasing, one bin per orbital period was used as input to the epoch folding. This then

yielded peaks at 4 and 8 times the orbital period. A visual inspection of Figure 2 verifies that this long-term period is real: there are prominent oscillations around MJD 52000 which have a period  $\sim 4$  times the orbital period.

Fig. 3 shows the 5-12.1 keV orbital light curves when the the total time period is divided into three different intensity levels based on the average count rate per orbit: bright (average count rate per orbit greater than 2 c/s); medium (average count rate per orbit in range 1.5-2 c/s) and dim (average count rate per orbit less than 1.5 c/s). The variability in the shape of the light curve for GX301-2 between bright, medium and dim levels is primarily due to variability in the outburst peak near orbital phase 0.9. The medium and dim level folded light curves are consistent with each other between orbital phases 0.1 to 0.8, and the bright level light curve is different from medium and dim between orbital phases 0.3 to 0.55.

Column densities were extracted from the RXTE/PCA spectral fits of Mukherjee and Paul (2004). The values used were the column densities of the absorbed component, since that measures the column density to the neutron star. Whereas the column densities of the scattered component are complicated to interpret and represent mean values to the scattering region. The orbital phase coverage of the RXTE/PCA column densities is not very uniform, and all column densities are from a single orbit observation of GX301-2. To obtain better orbital coverage and to cover the same multiyear timespan as the ASM lightcurve observations, an estimate of column density versus orbital phase was created based on the 3-5 keV to 5-12 keV softness ratio of the ASM observations. Conversion coefficients from the softness ratio to column density were determined using NASA’s WebPIMMS software assuming a power law spectrum with photon index -1.0. Figure 4 shows the derived ASM column densities compared to the observed PCA column densities. The main approximation in calculation of column densities from ASM softness ratio is use of a single power law spectrum, which is the equivalent of ignoring the scattering contribution to the spectrum.

### 3. Model

#### 3.1. Wind Model

The stellar wind velocity and density profiles are considered first. Both radial and azimuthal velocity components of the wind were included in this analysis. The radial wind velocity follows a power law and is taken to be of the form,  $v_w(r) = v_o(1 - R_s/r)^\beta + c_s$  with  $\beta = 1$ ,  $c_s$  the speed of sound and  $v_o$  the terminal velocity of the wind, (Castor et al 1975). Conservation of angular momentum dictates that the azimuthal component of the wind velocity drops off as  $1/r$ . The constant stellar angular speed  $\omega$  of WRAY977 is expressed

using the parameter  $f$ :

$$\omega(f) = f \times \omega_{\text{orb}} + (1 - f) \times \omega_{\text{per}} \quad (1)$$

with  $\omega_{\text{orb}}$  is the average orbital angular velocity ( $2\pi/P_{\text{orb}}$ ) and  $\omega_{\text{per}} = \omega_{\text{orb}}(1+e)^{0.5}/(1-e)^{1.5} = 3.06\omega_{\text{orb}}$  is the periastron angular velocity. Thus the primary is taken to be rotating at some angular velocity between  $\omega_{\text{orb}}$  and  $\omega_{\text{per}}$ . The large difference in  $\omega_{\text{orb}}$  and  $\omega_{\text{per}}$  is due to the high eccentricity of the orbit. Fits of a wind driven accretion model for GX301-2 were studied by L02 and found to be unable to fit the "double bump" nature of the light curve. As well L02 tested a wind and disk model of accretion for GX301-2 which could not fit the observations. The conclusion drawn by L02 was that a wind and stream model (Stevens 1988) is the best supported model for GX301-2.

### 3.2. Wind plus stream model

Simplified models describing a simultaneous wind and stream accretion process were first used by Haberl (1991) (straight line stream) and Leahy (1991) (spiral stream) to fit the less complete data from EXOSAT and TENMA. In the model (Stevens 1988), a stream originates at the point on the surface of WRAY 977 that is nearest to GX301-2. The stream then bends backwards (with respect to the direction of orbital velocity of GX301-2) as it travels radially outward from the primary star.

Here we calculate the stream position at any given orbital phase by integrating the radial and azimuthal equations of motion. Roughly speaking the stream is like an Archimedes spiral co-rotating at the orbital angular velocity. However since the point of origin of the stream follows the neutron star it has a greatly varying angular velocity, by a factor of  $[(1+e)/(1-e)]^2 = 7.4$  for GX301-2. The result is a stream that changes shape considerably with orbital phase, similar to a garden sprinkler with an uneven rotational speed. Animations of the stream can be found at [www.iras.ucalgary.ca/~leahy/](http://www.iras.ucalgary.ca/~leahy/). The stream shape depends on the terminal wind velocity ( $v_o$ ), the angular speed ( $\omega(f)$ ) of WRAY 977, the system inclination, and on companion radius (through the wind law). The model light curve depends also on the stream width and density and the speed of sound. In order to calculate the full stream shape we started with a set of terminal wind velocities and stellar angular velocities ( $f$ ) then created a stream for each combination of  $v_o$  and  $f$ . To allow  $v_o$  and  $f$  to be free parameters, the stream position was interpolated in  $f$  and  $v_o$ .

Analysis done by L02 suggests that two crossing points (with orbital phases  $\gamma_1, \gamma_2$ ) between GX301-2 and the stream exist. While L02 allowed  $\gamma_1, \gamma_2$  to be free parameters, here we constrain them to be governed by the computed stream shape. The relative velocity of GX301-2 with respect to the stream and the stream density both play a large role in the

intensity of the X-ray flux. One stream crossing occurs just before periastron (orbital phase  $\sim 0.93$ ). GX301-2 is nearing its peak speed to overtake the stream, but the stream is near its highest density and lowest radial velocity resulting in a large increase in luminosity. The second stream crossing is at orbital phase  $\sim 0.55$ . As GX301-2 approaches apastron it slows to its most leisurely pace, so the stream is able to overtake the neutron star. Since the radial wind speed is highest and stream density lowest at apastron, a significantly lower peak in luminosity occurs. Physically one expects the stream width to increase with radial distance from the companion star, due to expansion of the higher density, overpressured stream in the lower density surrounding stellar wind. Here we use a Gaussian density profile with variable width. The angular width ( $\sigma$ ) is taken as a power law function of distance from the center of the companion star:  $\sigma(r) = \sigma_0(r/r_{per})^{-\kappa}$ , with  $\sigma_0$  the width normalized at periastron distance  $r_{per}$ .  $\kappa < 0$  corresponds to a stream with increasing physical width as the stream propagates outward. We ensure mass conservation by employing the continuity equation, so the density of the stream varies with  $r$  depending on the value of  $\kappa$ . The angular width of the stream (viewed from the companion star) depends on  $(r/r_{per})^{-\kappa-1}$ , so  $\kappa > -1$  corresponds to a stream with decreasing angular width as the stream propagates outward.

### 3.3. Comparison to Data

GX301-2 has a significant absorption by its stellar wind in soft X-rays with column densities several times  $10^{23} \text{ cm}^{-2}$ . This shows up well in Fig. 1 above: Band 1 and Band 2 data are affected significantly by absorption but Band 3 (5-12.1 keV) is mostly free of absorption effects since the photoelectric cross-section is very small above 3-4 keV. This is also confirmed by the consistency in shape of the Band 3 light curve with the BATSE light curve (Koh et al. 1997), although the RXTE/ ASM light curve here is of significantly better statistical quality. Thus the 5-12.1 keV band flux is taken here to be proportional to the X-ray luminosity of the pulsar.

The comparison of our wind plus stream models to the RXTE/ ASM orbital light curve is made by  $\chi^2$  minimization using the non-linear conjugate gradient method. For each minimization (i.e. fitting), some parameters were taken as fixed parameters (stellar radius and system inclination) and the remaining parameters were taken as free parameters.

The mass-radius constraints on WRAY 977 were discussed in detail in L02. Here we replot the radius constraints in Fig. 5. We use inclination rather than mass as the independent variable, since radius and inclination are critical inputs to our model calculations. Also we have extended the upper limit of  $T_{eff}$  to 22500 K as suggested by the data of Kaper et al. (1995), and show the most relevant region of the radius vs. inclination diagram. Allowable

companion radii are smaller than those that result in eclipses (i.e. left of the "Eclipse Limit" line) and smaller than those that overflow the Roche lobe (below the "Mean Roche Radius" line). These are hard constraints that cannot be violated. The estimated mass-radius relation and estimated  $T_{eff}$  give that the star should fall in between the  $T_{eff}=20000$  K and 22500 K lines. Thus for our models, we chose allowable inclination and radius pairs falling in the allowed region from Fig. 5. We find a maximum radius of  $78 R_{\odot}$  consistent with the maximum of (Kaper et al. 1995), and a minimum radius of  $45 R_{\odot}$ . These correspond to inclinations of  $52^{\circ}$  and  $77.5^{\circ}$ .

Different pairs of stellar radii and inclination were chosen covering the allowed region in the radius-inclination plane. These are listed in the first two columns of Table 1. For each case of the two fixed parameters;  $R_c$  and inclination, the stream model was fit to the ASM data. The free parameters in the model were terminal wind velocity ( $v_o$ ), stream density contrast ( $ds$ ), stream angular width in radians ( $\sigma_o$ ), stream width variation parameter  $\kappa$ , mass-loss rate ( $\dot{m}$ ), a normalization factor, and the stellar angular velocity factor ( $f$ ) that determined the rate of rotation of WRAY 977. Initial fits were done on the light curves and column densities from the full ASM data set, then fits were carried out on the three subsets of lightcurve and column density data for the different intensity levels (bright, medium and dim). Since the light curves for the three different intensity levels were significantly different, we present results for separately fitting the different intensity levels. We carried some joint fits to both lightcurve and column density, and found no significant difference to fits done to lightcurve to determine all model lightcurve parameters, followed by fits to column density to determine wind mass loss rate. This is not too surprising as the errors on lightcurve data are very small, whereas the errors on the column density data are large (see Fig.3 and Fig.4). Thus the the light curve completely dominated the determination of joint parameters. The second procedure has the two advantages of: much faster run-time; and less reliance on the approximate column densities.

#### 4. Results

For each set of fixed parameters (radius,  $R_c$ , and inclination  $inc$ ) in Table 1), the best fit parameters for fitting to the ASM light curve and column density data are listed in Table 1. B, M and D refer to bright, medium and dim intensity levels. The fit parameters for the light curve fits are base wind velocity ( $v_{wo}$ ), stellar angular velocity parameter ( $f1$ ), stream width and width variation parameters ( $\sigma_o$  and  $\kappa$ ), and stream central density enhancement at periastron ( $ds$ ). The  $\chi_L^2$  values for the light curve fits are listed in column 8. The large  $\chi_L^2$  compared to the number of degrees of freedom (34) shows that the model does not provide

a statistically good fit. Fig. 6 shows model fits to the ASM lightcurve data (top panel) and ASM column density data (bottom panel) for bright level for  $R_c = 75R_\odot$ , inclination  $55^\circ$ . The shape of the light curve is fit very well: the contributions to  $\chi_L^2$  mainly come from real fluctuations in the observed light curve at orbital phases  $\sim 0.3$ -  $0.4$  and  $\sim 0.6$  -  $0.7$ . This is likely due to clumps in the stellar wind and stream that we cannot model currently: Mukherjee and Paul (2004) also noted large fluctuations in their RXTE/PCA observations which they attributed to clumps in the stellar wind.

There are several trends in the fit results. As one goes to smaller  $R_c$  and larger inclination, the best fit wind velocity decreases: from  $\sim 600$  km/s to  $\sim 300$  km/s. The derived windspeeds are in good agreement with the values estimated from the optical spectrum of WRAY 977 (Kaper et al. (1995)). In all cases, for a given  $R_c$  and inclination, the wind velocity is highest for bright and lowest for dim. Also in all cases the best fit mass-loss rate is highest for bright and similar for medium and dim, where as the density enhancement ratio,  $ds$ , is smallest for bright and highest for medium. Instead, one can consider the central density of the stream (proportional to density enhancement ratio, column 7, times mass-loss rate, column 9) This shows that the central density of the stream is essentially unchanged between bright and medium levels, so the main change between bright and medium is the stellar wind mass-loss rate. However the central density of the stream drops from medium to dim whereas the wind mass-loss rate does not change significantly. Thus the main change between medium in dim is that the stream density is lower for dim.

The angular rotation rate parameter  $f1$  systematically decreases with  $R_c$ . From the stream model, this is just due to the requirement of having the neutron star- stream crossings at the correct observed orbital phases as the position of the base of the wind (at  $R_c$ ) changes. From equation 1, a value of  $f1=1$  is for the companion rotation synchronous with the mean orbital rotation and a value of 0 is for synchronous with periastron angular velocity. Tidal torques in the eccentric orbit would yield an intermediate value, consistent with the best-fit values in Table 1.

Values of  $\kappa$  are in the range  $-0.4$  to  $0$ , thus the stream physical width grows with  $r$ , as expected, and the stream angular width decreases with  $r$  ( $-1 < \kappa < 0$ ). The stream density enhancement over that of the spherical component of the stellar wind is typically 25 (with a range of 20 to 30), and the stream angular width at periastron is in the range of  $22^\circ$  to  $26^\circ$ .

The column density model gives two gradual peaks (see Fig. 6): one near periastron and one near orbital phase 0.25. The stream is seen to dominate over the wind component for the periastron peak but both wind and stream contribute roughly equally for the peak near phase 0.25. The system inclination can be such that the neutron star is nearly eclipsed by the companion (see Fig. 5 for  $R_c$ -inclination values where this occurs, near the "Eclipse



Limit” line). In this case the wind contribution to the column density becomes large near orbital phase 0.25, when the line-of-sight passes near the companion’s surface, and the  $\chi^2_N$  for the column density fit becomes large. An example of this is the  $(48R_\odot, 75^\circ)$  case in Table 1.

Finally, we have calculated the mass-loss rate in the stream and added this as column 10 in Table 1. It is seen that the stream mass-loss rate is about a factor of 2 to 2.5 times higher than the mass-loss rate in the wind. This is a dramatic confirmation of the importance of the stream in the total mass-loss rate from WRAY 977. It is also consistent with WRAY 977 being close to filling its Roche lobe. Since this can only occur at lower inclinations without having WRAY 977 too close to eclipsing, this is another indicator that the system inclination is near the low end of the allow range (near  $\sim 55^\circ$ ).

## 5. Conclusion

Long term (10-year) monitoring of GX301-2 with the RXTE/ASM has revealed some new properties of this high-mass X-ray binary. Secular changes in flux (Fig. 2) are also accompanied by flux oscillations with a period of four 41.5-day binary orbits. The orbital light curve is seen to be significantly different between bright, medium and dim flux levels (Fig.3).

We have constructed an improved stellar wind and stream model for the GX301-2/WRAY 977 binary system, extending the work of L02. The model is compared to long term lightcurve observations from the RXTE/ASM and to column densities derived from the RXTE/ASM 3-5 keV to 5-12 keV softness ratios. We have validated the necessity of including a stream in the mass flow from WRAY 977 in addition to a spherically symmetric wind in order to explain the observed light curves and column densities. The timings and amplitudes of the two peaks in the lightcurve, near orbital phases 0.92 and 0.5 are naturally explained by accretion onto the neutron star from an Archimedes spiral-type stream. The quality of the column density data is low due to statistical uncertainties. Yet the column density data provides the primary constraint on the stellar wind mass loss rate. We have found best fit parameters for a range of radii for WRAY 977 and a range of system inclinations which are consistent with the physical constraints such as no eclipse and maximum mean radius not exceeding the mean Roche radius (see Fig. 5). From the model fits, we find the change between bright and medium intensity levels is primarily due to decreased mass loss in the stellar wind, but the change between medium and dim intensity levels is primarily due to decreased stream density. For any intensity level, the total mass-loss rate in the stream exceeds that in the wind by a factor of  $\sim 2.5$ , indicating the crucial role of the stream in this

binary system.

The model fits at higher inclinations are significantly worse than those at lower inclinations. In Table 1, last column, we list the total  $\chi^2$  (values for lightcurve and column density fits summed). The best fit values of  $(R_c, inc)$  can be determined by summing the total  $\chi^2$  for the three intensity levels B, M and D to yield a total  $\chi_{BMD}^2$ . This gives, in order of increasing  $\chi_{BMD}^2$ ,  $(R_c, inc) = (75R_\odot, 55^\circ)$  with  $\chi_{BMD}^2 = 1660$ ;  $(68R_\odot, 60^\circ)$  with  $\chi_{BMD}^2 = 1820$ ; and  $(62R_\odot, 60^\circ)$  with  $\chi_{BMD}^2 = 2010$ . Thus the  $\chi_{BMD}^2$  from our modeling strongly prefers the lowest inclination. In Table 2, we have listed the companion mass vs. inclination for GX301-2. Thus the wind plus stream model fits to the RXTE/ASM lightcurve and column density data favor  $\sim 55 - 60^\circ$  inclination, or companion mass  $\sim 53 - 62M_\odot$ .

### Acknowledgments

DAL acknowledges support from the Natural Sciences and Engineering Research Council.

### REFERENCES

- Aurière, M. 1982, A&A, 109, 301
- Canizares, C. R., Grindlay, J. E., Hiltner, W. A., Liller, W., and McClintock, J. E. 1978, ApJ, 224, 39
- Castor, J., Abbott, D. and Klein, R. 1975, ApJ, 195, 157
- Djorgovski, S., and King, I. R. 1984, ApJ, 277, L49
- Haberl, F. 1991, ApJ, 376, 245
- Hagiwara, K., and Zeppenfeld, D. 1986, Nucl.Phys., 274, 1
- Harris, W. E., and van den Bergh, S. 1984, AJ, 89, 1816
- Hénon, M. 1961, Ann.d’Ap., 24, 369
- Kaper, L., Lamers, H., Ruymaekers, E., van den Heuvel, E., & Zuiderwijk, E. 1995, A&A, 300, 446
- King, I. R. 1966, AJ, 71, 276

Table 1: Best Fit Parameters.

$(R_c, inc)$	Data	$v_{wo}$ [km/s]	$f1$	$\sigma_o$	$\kappa$	$ds$	$\chi_L^2$	$\dot{m}_{wind}$ [ $M_\odot/yr$ ]	$\dot{m}_{stream}$ [ $M_\odot/yr$ ]	$\chi_N^2$	Total $\chi^2$
$(75R_\odot, 55^\circ)$	B	630	0.44	0.44	-0.40	25	430	$3.8 \times 10^{-5}$	$9.2 \times 10^{-5}$	140	570
	M	600	0.48	0.43	-0.31	31	690	$3.0 \times 10^{-5}$	$8.6 \times 10^{-5}$	99	790
	D	580	0.51	0.46	-0.31	26	210	$2.7 \times 10^{-5}$	$7.4 \times 10^{-5}$	88	300
$(68R_\odot, 60^\circ)$	B	570	0.38	0.43	-0.32	22	460	$3.4 \times 10^{-5}$	$6.9 \times 10^{-5}$	160	620
	M	540	0.42	0.42	-0.23	28	750	$2.6 \times 10^{-5}$	$6.4 \times 10^{-5}$	130	880
	D	500	0.45	0.45	-0.23	24	230	$2.2 \times 10^{-5}$	$5.3 \times 10^{-5}$	89	320
$(62R_\odot, 70^\circ)$	B	500	0.35	0.43	-0.28	22	500	$1.2 \times 10^{-5}$	$2.4 \times 10^{-5}$	490	990
	M	470	0.39	0.42	-0.19	28	780	$7.3 \times 10^{-6}$	$1.8 \times 10^{-5}$	550	1300
	D	450	0.41	0.44	-0.20	24	250	$8.8 \times 10^{-6}$	$2.0 \times 10^{-5}$	170	420
$(62R_\odot, 65^\circ)$	B	510	0.32	0.42	-0.24	21	530	$2.6 \times 10^{-5}$	$4.8 \times 10^{-5}$	220	750
	M	480	0.39	0.42	-0.15	26	820	$1.9 \times 10^{-5}$	$4.4 \times 10^{-5}$	210	1000
	D	450	0.39	0.44	-0.17	23	250	$1.7 \times 10^{-5}$	$3.8 \times 10^{-5}$	100	350
$(62R_\odot, 60^\circ)$	B	520	0.29	0.42	-0.19	20	570	$3.4 \times 10^{-5}$	$6.0 \times 10^{-5}$	140	710
	M	480	0.34	0.41	-0.10	25	860	$2.5 \times 10^{-5}$	$5.3 \times 10^{-5}$	100	960
	D	450	0.36	0.45	-0.13	22	260	$2.2 \times 10^{-5}$	$4.9 \times 10^{-5}$	84	340
$(55R_\odot, 70^\circ)$	B	450	0.22	0.41	-0.13	20	650	$1.6 \times 10^{-5}$	$2.7 \times 10^{-5}$	380	1000
	M	420	0.28	0.40	-0.05	25	930	$9.7 \times 10^{-6}$	$1.9 \times 10^{-5}$	440	1400
	D	390	0.30	0.44	-0.08	22	300	$9.9 \times 10^{-6}$	$2.1 \times 10^{-5}$	140	440
$(51R_\odot, 70^\circ)$	B	430	0.15	0.40	-0.05	19	740	$1.7 \times 10^{-5}$	$2.6 \times 10^{-5}$	330	1100
	M	400	0.20	0.40	+0.02	24	1000	$1.1 \times 10^{-5}$	$2.1 \times 10^{-5}$	390	1400
	D	370	0.17	0.43	-0.02	21	330	$1.0 \times 10^{-5}$	$1.9 \times 10^{-5}$	130	460
$(48R_\odot, 75^\circ)$	B	410	0.09	0.39	-0.005	19	840	$3.4 \times 10^{-6}$	$4.9 \times 10^{-6}$	710	1600
	M	380	0.15	0.39	+0.07	23	1110	$1.6 \times 10^{-6}$	$2.8 \times 10^{-6}$	740	1900
	D	350	0.17	0.43	+0.01	21	370	$2.4 \times 10^{-6}$	$4.7 \times 10^{-6}$	250	620

Table 2: Mass and Inclination.

$inc$	$55^\circ$	$60^\circ$	$65^\circ$	$70^\circ$	$75^\circ$
$M_c$	$62M_\odot$	$53M_\odot$	$47M_\odot$	$42M_\odot$	$39M_\odot$

- King, I. R. 1975, *Dynamics of Stellar Systems*, A. Hayli, Dordrecht: Reidel, 1975, 99
- King, I. R., Hedemann, E., Hodge, S. M., and White, R. E. 1968, *AJ*, 73, 456
- Koh, D., Bildsten, L., Chakrabarty, D. et al. 1997, *ApJ*, 479, 933
- Kron, G. E., Hewitt, A. V., and Wasserman, L. H. 1984, *PASP*, 96, 198
- Leahy, D. 2002, *A&A*, 391, 219
- Leahy, D., 1999, *JRASC.*, 93, 33
- Leahy, D., Creighton, J., 1993, *MNRAS.*, 263, 314
- Leahy, D., 1991, *MNRAS.*, 250, 310
- Leahy, D. & Matsuoka, M. 1990, *ApJ*, 355, 627
- Leahy, D.A., Matsuoka, M., Kawai, N. & Makino, F. 1989, *MNRAS*, 236, 603
- Leahy, D.A., Matsuoka, M., Kawai, N. & Makino, F. 1989, *MNRAS*, 237, 269
- Leahy, D.A., Elsner, R., & Weisskopf, M. 1983, *ApJ*, 272, 256
- Levine, A., Bradt, H., Cui, W., et al. 1996, *ApJ*, 469, L33
- Lynden-Bell, D., and Wood, R. 1968, *MNRAS*, 138, 495
- Mukherjee, U. and Paul, B. 2004, *A&A*, 427, 567
- Newell, E. B., and O’Neil, E. J. 1978, *ApJS*, 37, 27
- Ortolani, S., Rosino, L., and Sandage, A. 1985, *AJ*, 90, 473
- Parkes, G., Mason, K., Murdin, P. & Culhane, J. 1980, *MNRAS*, 191, 547
- Peterson, C. J. 1976, *AJ*, 81, 617
- Pravdo, S., Day, C., Angelini, L., et al. 1996 *ApJ*, 454, 872
- Saraswat, P., Yoshida, A., Mihara, T. et al. 1996, *ApJ*, 463, 726
- Sato, N., Nagase, F., Kawai, N., et al. 1986 *ApJ*, 304, 241
- Shaller, G., Schaerer, D. & Maeder, G. 1992, *A&AS*, 96, 269

Spitzer, L. 1985, Dynamics of Star Clusters, J. Goodman and P. Hut, Dordrecht: Reidel, 109

Stevens, I. R. 1988 MNRAS, 232, 199

Watanabe, S., et al. 2003, ApJ, 597, L37

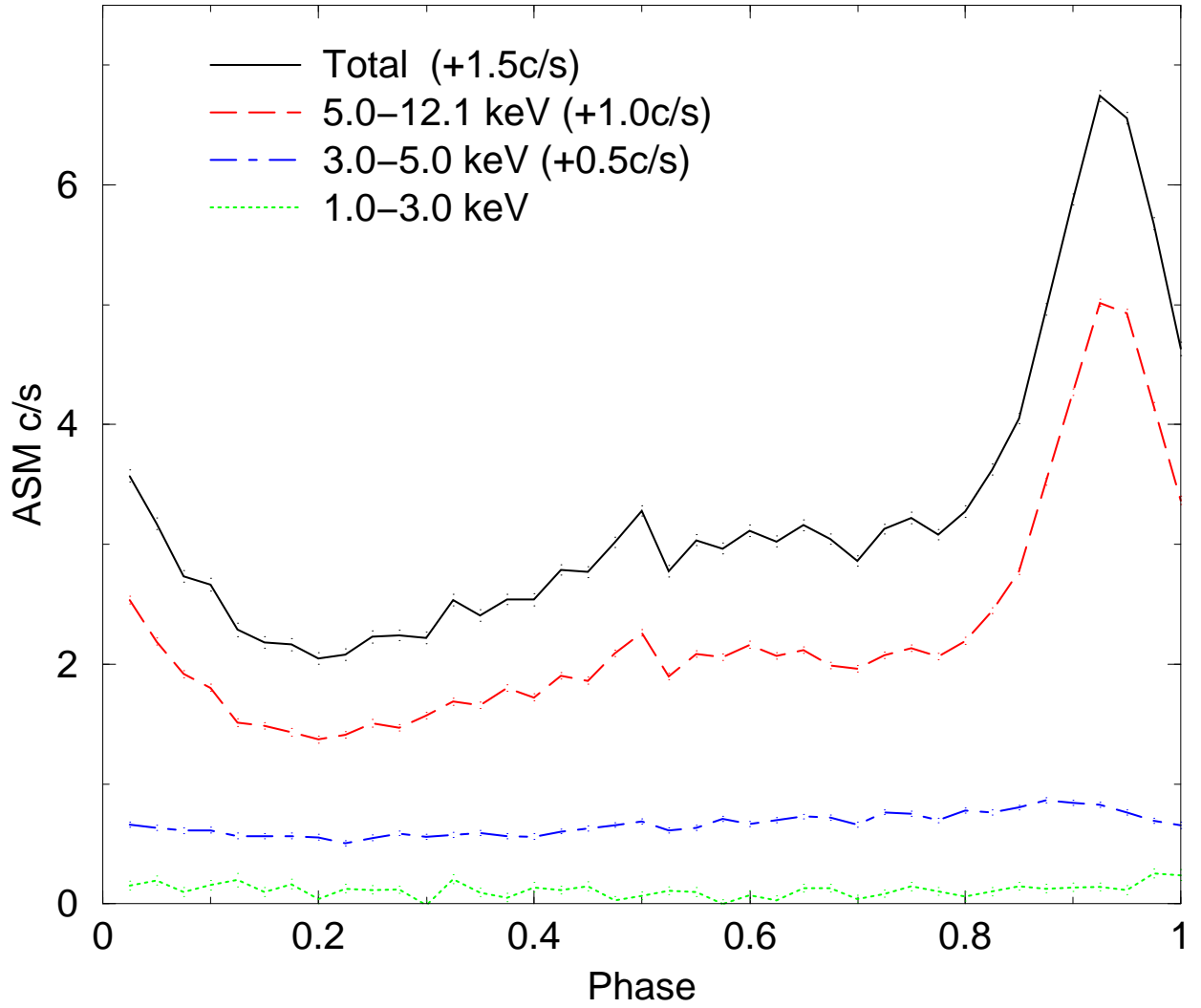


Fig. 1.— Orbital light curves of GX301-2 in the three RXTE/ ASM energy bands and total energy band from the ASM dwell data folded at 41.498 days.

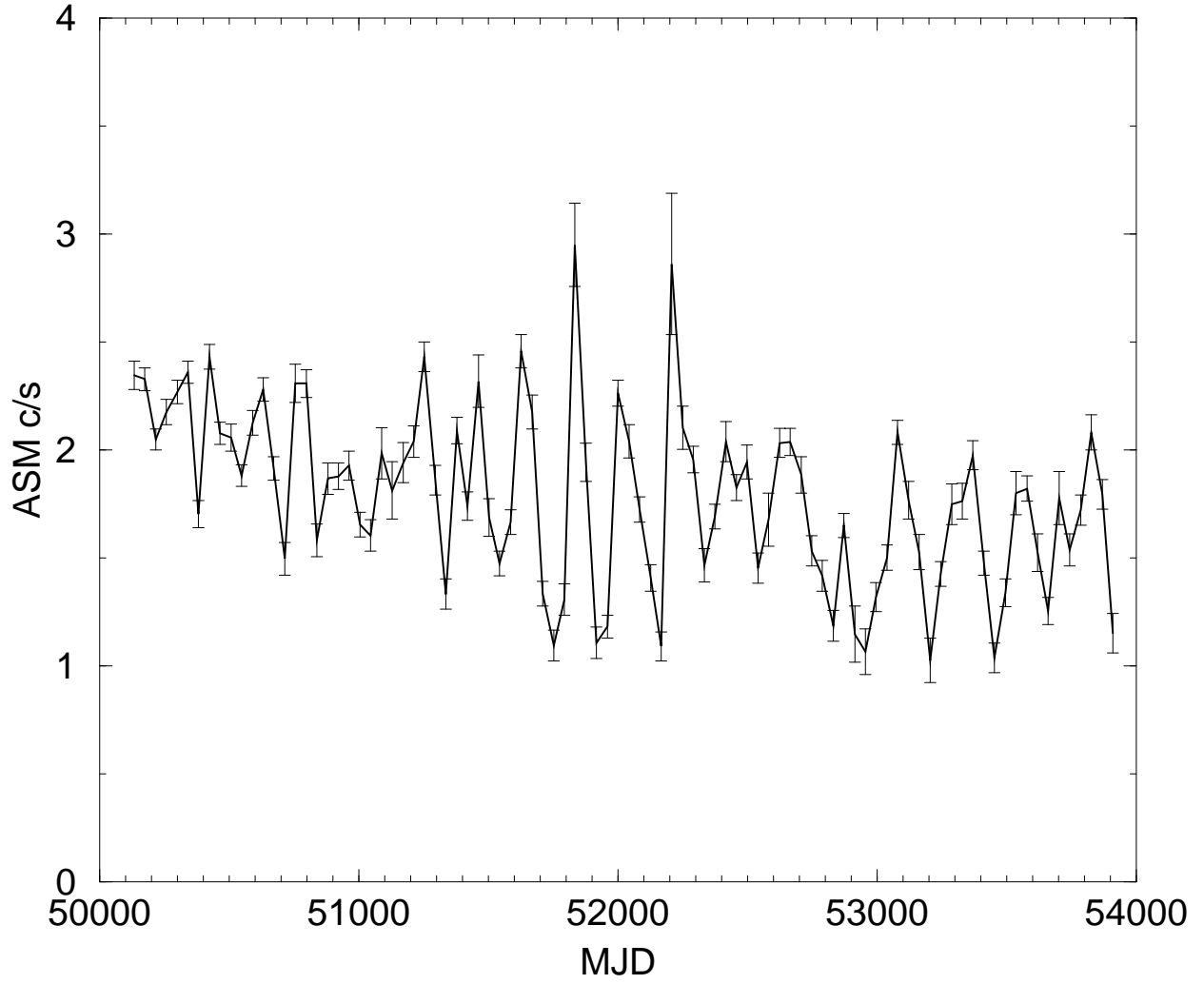


Fig. 2.— Long term variability: RXTE/ ASM data for the entire observation period with timebins equal to one orbital period (41.498 days).

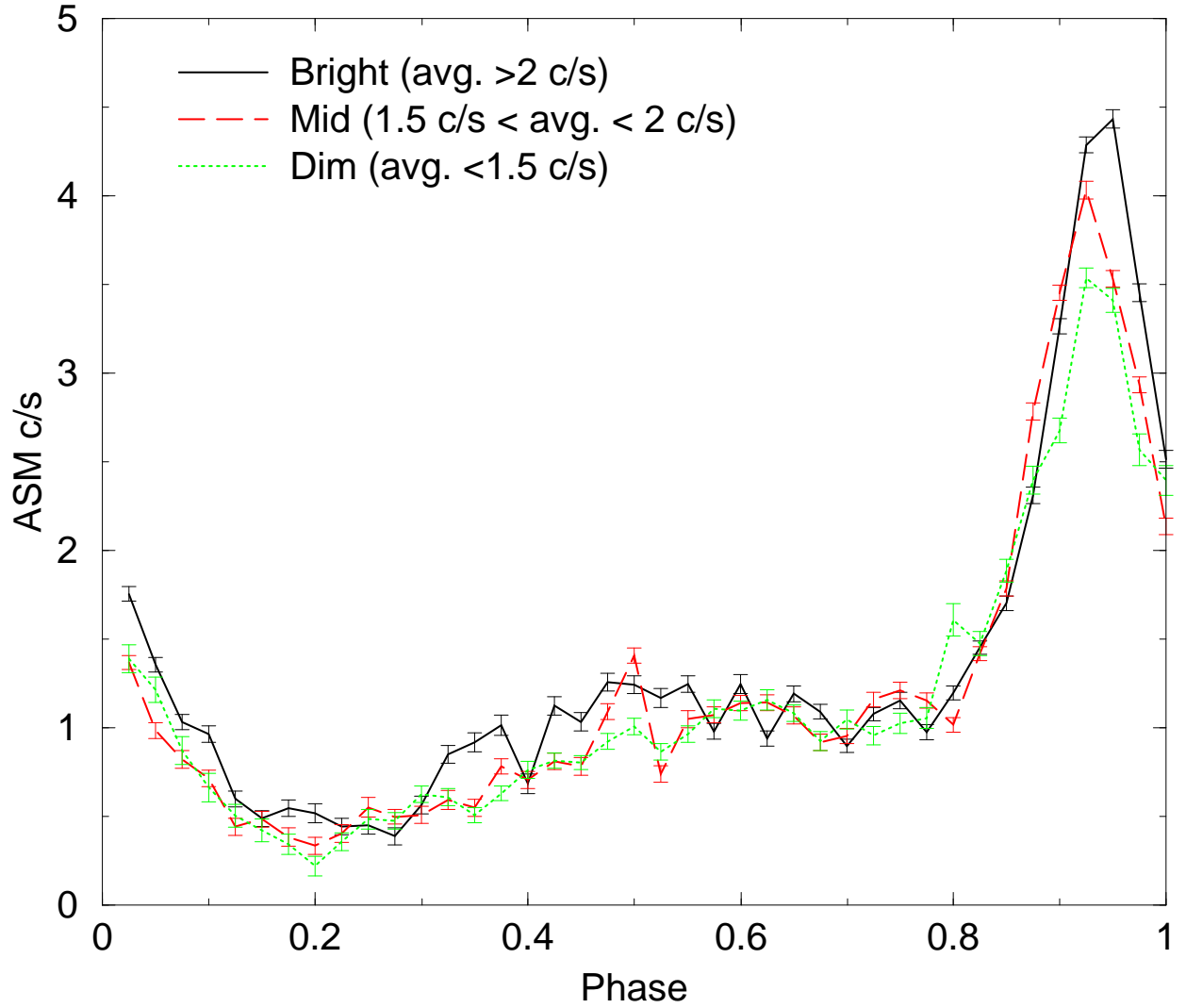


Fig. 3.— 5-12.1 keV orbital light curves for bright (average count rate per orbit greater than 2 c/s); medium (average count rate per orbit in range 1.5- 2 c/s) and dim (average count rate per orbit less than 1.5 c/s).



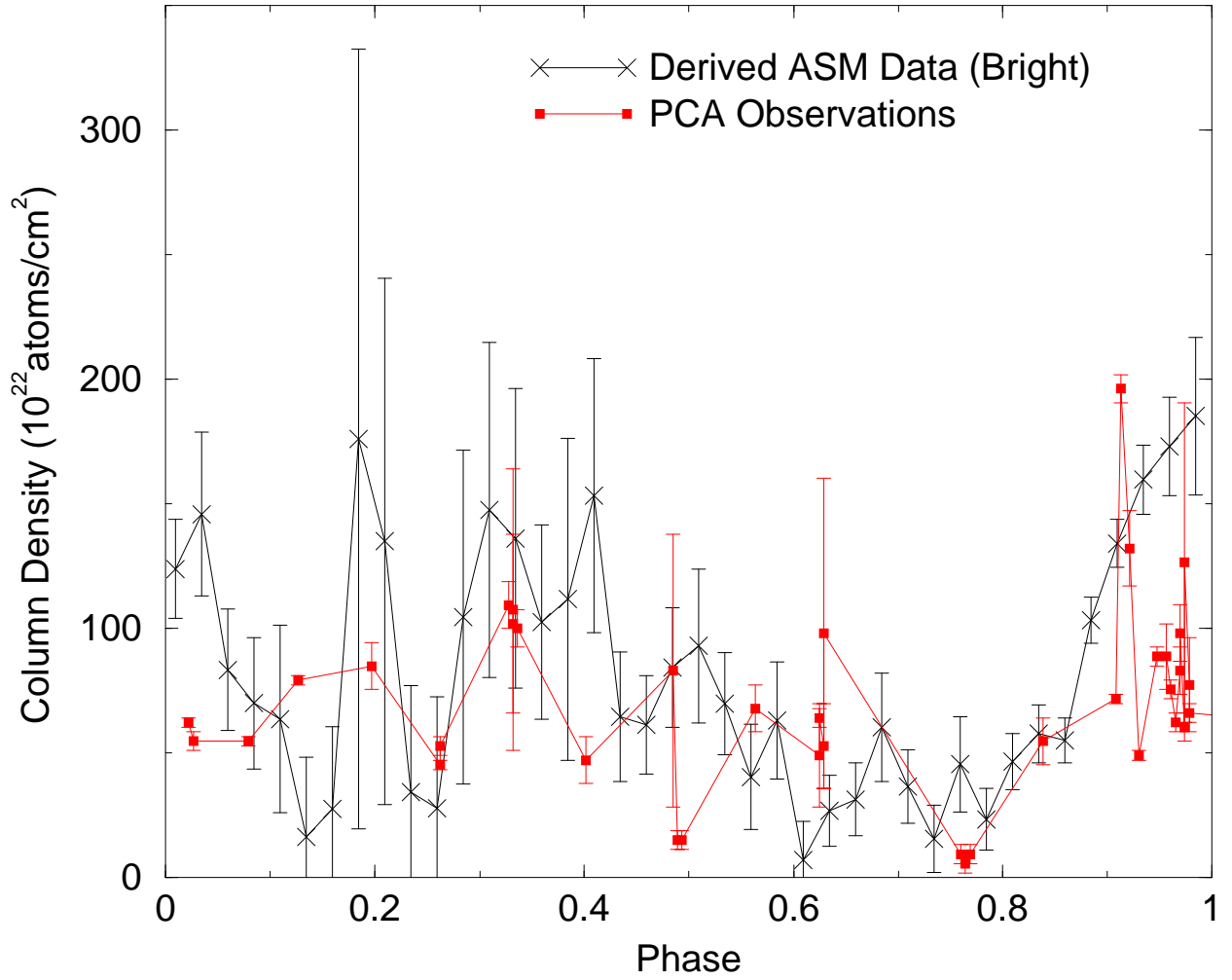


Fig. 4.— Column densities derived from ASM 3-5 keV to 5-12 keV softness ratio for bright level data, compared to the observed PCA column densities.

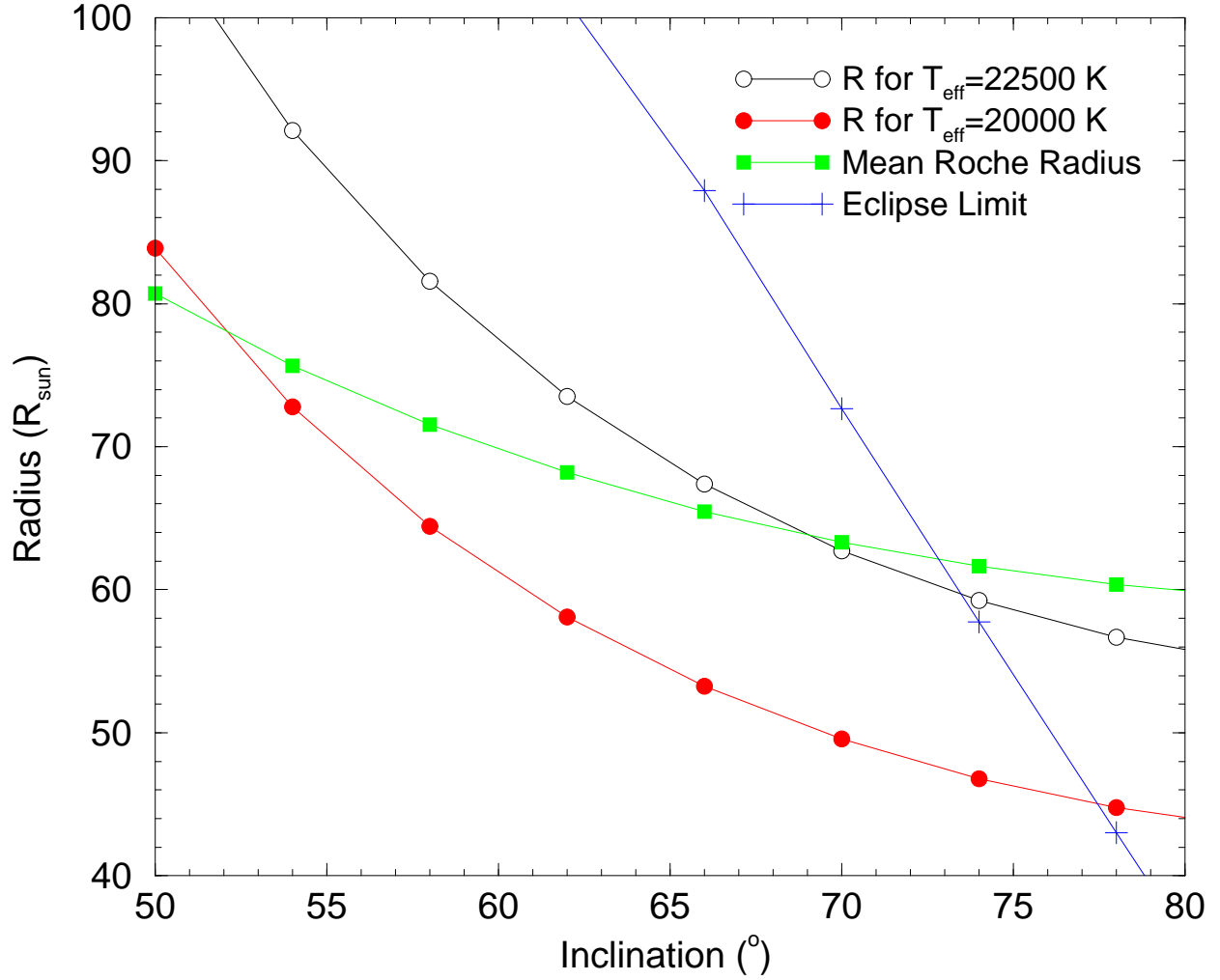


Fig. 5.— Radius- orbital inclination constraints on WRAY 977. Absence of eclipse gives an allowed region is left of the "Eclipse Limit" line; WRAY 977's mean radius is less than the "Mean Roche Radius"; mass-radius relations for upper and lower limits to  $T_{\text{eff}}$  are plotted: the allowed region is between these two lines.

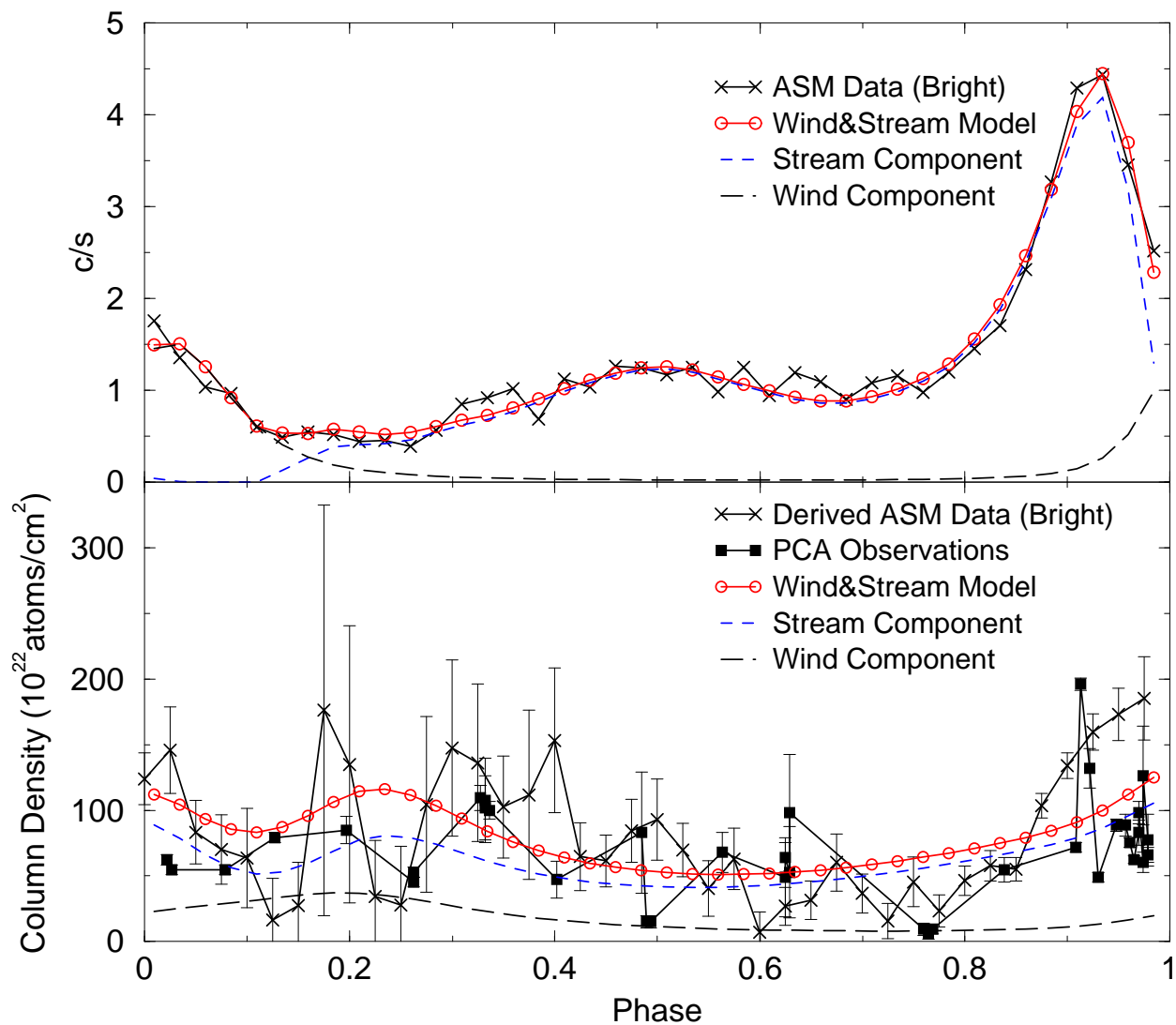


Fig. 6.— Model fits to ASM lightcurve data (top panel) and column density data (bottom panel) for bright level for  $R_c = 75R_\odot$ , inclination  $55^\circ$ . The contributions to light curve and column density from wind and stream are shown separately, as well as the total.